Applied Surface Science 364 (2016) 573–578

Contents lists available at ScienceDirect

Applied Surface Science

journal homepage: www.elsevier.com/locate/apsusc

Ytterbium oxide nanodots via block copolymer self-assembly and their efficacy to dye-sensitized solar cells

Kwang-Won Park[a], Sungwoo Ahn[a], Sung-Hwan Lim[a], Ming Hao Jin[a], Jeemin Song[a], Seung-Young Yun[a], Hyeon Mo Kim[b], Gi Jeong Kim[b], Kang Min Ok[a], Jongin Hong[a,*]

[a] Department of Chemistry, Chung-Ang University, 84 Heukseok-ro, Dongjak-gu, Seoul 156-756, Republic of Korea
[b] Sooyang Chemtec Co., Ltd., Digital-ro 32-gil, Guro-gu, Seoul 152-777, Republic of Korea

ARTICLE INFO

Article history:
Received 23 September 2015
Received in revised form 4 December 2015
Accepted 10 December 2015
Available online 13 December 2015

Keywords:
Ytterbium oxide
Block copolymer
Spectral converter
Dye-sensitized solar cell

ABSTRACT

In this study, we develop a novel phosphor, Yb_2O_3, to be used as the spectral converter in dye-sensitized solar cells (DSSCs) for the efficient capture of ultraviolet light via down-conversion. These zero-dimensional nanodots with a high refractive index also allow more light to be trapped and can prevent charge recombination at the interfaces in the DSSCs. Compared to DSSCs without the nanodots, the DSSCs fabricated with the Yb_2O_3 nanodots exhibits higher power-conversion efficiencies for both the N719 (10.5%) and CSD-01 (20.5%) dyes. The multifunctionality of the Yb_2O_3 nanodots provides a new route for improving the performance of DSSCs.

1. Introduction

To aid the efforts of those researching clean and sustainable energy sources against a backdrop of the impending depletion of fossil fuels and the global warming crisis, photovoltaic devices have been extensively studied across the world. Since O'Regan and Grätzel invented a dye-sensitized solar cell (DSSC) in 1991 [1], it has attracted much attention because of its distinctive features, such as its color and transparency, low weight, flexibility, workability under low light conditions, and easy integration with buildings and automobiles [2,3]. The DSSC is a photoelectrochemical device that mimics the principles of natural photosynthesis, and its photocurrent is generated at the interface between the photosensitized semiconductors and redox electrolytes under solar illumination. To date, the many attempts to enhance its performance have mainly been focused on developing photosensitizers with a wider spectral absorption band and higher molar extinction coefficients [4–6]. Another interesting approach is applying efficient photon management to increase the light harvesting efficiency (LHE) of the cell. Most of this work has focused on increasing the optical path length or local electromagnetic energy within the absorbing electrode [7–10]. However, the harvesting of ultraviolet (UV) and near-infrared (NIR) light is still difficult because most of the photosensitizers used in DSSCs only absorb light with wavelengths ranging from 400 to 800 nm. Recently, to maximize the usage of solar photons, luminescent materials based on trivalent lanthanide ions have been considered as spectral converters because of their rich energy-level structure (known as the Dieke diagram) [11]. For example, Wu et al. demonstrated that the rare-earth compound YF_3:Eu^{3+} could be used as a UV-absorbing spectral converter to improve the DSSC performance via down-conversion, in which one UV photon is transformed into two visible photons [12]. On the other hand, Zhang et al. reported $NaYF_4$:Yb^{3+},Er^{3+} nanoparticles that can improve the DSSC performance via up-conversion, which extends the spectral response range to the infrared region [13]. Despite recent progress in preparing such fluorides, the synthesis of high-quality nanocrystals still requires complicated processes and high reaction temperatures.

Recently, arrays of zero-dimensional nanoparticles with high refractive indices have been adopted to confine light in the propagation direction, and thus, such nanoparticles can be employed to trap the incident sunlight in a solar cell [14]. To prepare self-ordered nanomaterials on solid substrates, block copolymers (BCPs), which consist of two or more chemically different polymers covalently connected, have been extensively exploited [15–17]. In particular, BCP micelles, in which a solvophilic block forms a swollen corona around a solvophobic core, have been utilized as templates for inorganic nanomaterials, including metals, semiconductors, and ceramics. The precursors of such inorganic materials are incorporated into the micellar core, then the micellar films are

* Corresponding author.
E-mail address: hongj@cau.ac.kr (J. Hong).

http://dx.doi.org/10.1016/j.apsusc.2015.12.077
0169-4332/

formed on the substrate by either spin coating or dip coating, and finally the BCP templates are removed with UV exposure, O_2 plasma etching, or calcination. For example, Lohmueller et al. fabricated hexagonally ordered metal nanoparticles (Au, Pt, and Pd) on glass substrates by using polystyrene-block-poly(2-vinylpyridine) (PS-*b*-P2VP) micelles [18]. Anthony et al. reported the fabrication of two-dimensional arrays of luminescent metal-chalcogenide nanocrystals [19]. In addition, Kim et al. demonstrated the synthesis of TiO_2 and ferroelectric $PbTiO_3$ nanodot arrays on platinized silicon substrates by using polystyrene-block-poly(ethylene oxide) (PS-*b*-PEO) loaded with sol–gel precursors [20].

In this study, we developed a novel phosphor, Yb_2O_3, to be used as the spectral converter in DSSCs for the efficient capture of the full solar spectrum. We found that the Yb_2O_3 nanodots fabricated via the BCP self-assembly can trap more light and prevent charge recombination at the interfaces in the DSSCs.

2. Experimental methods

2.1. Preparation of ytterbium oxide nanodots

All of the chemicals were purchased from Sigma Aldrich and used without further purification. The poly(styrene-block-4-vinylpyridine) diblock copolymer (PS-*b*-P4VP, $M_{n,PS}$ = 41 kg/mol, $M_{n,P4VP}$ = 24 kg/mol, M_w/M_n = 1.06) was obtained from Polymer Source Inc. First, the PS-*b*-P4VP was dissolved in toluene at 80 °C and stirred for 2 h to yield a solution with a concentration of 0.5 wt.%. The Yb precursor solution (1.0 wt.%) was prepared by dissolving ytterbium(III) chloride hexahydrate ($YbCl_3{\cdot}6H_2O$) in ethanol. This solution was added to the BCP solution at different molar ratios of $YbCl_3{\cdot}6H_2O$ to 4VP (0.1, 0.3, and 0.5), and then the mixture was vigorously stirred for a week. The precursor-loaded inverse micelles were spin-coated onto transparent fluorine-doped SnO_2 (FTO)-coated conducting glass (TEC 8, Pilkington, 2.2-mm-thick, sheet resistance = 8 Ω/□) at 2000 rpm for 60 s. The polymer templates were eliminated with O_2 plasma etching at 80 W for 7 min, leaving the zero-dimensional ytterbium oxide nanodots on the substrate.

2.2. Characterization of the Yb_2O_3 nanodots

Non-contact atomic force microscopy (AFM, XE-120, Park Systems, Korea) was used to image the surface morphology of the prepared nanodots. Al-coated non-contact tips (Nanosensors, PPP-NCHR, Switzerland, force constant (k) = 42 N/m, resonance frequency = 330 kHz) were used for the AFM imaging, and the scan rate was 1.0 Hz. The optical transmittance spectra of the nanodots were collected with a UV/VIS/NIR spectrophotometer (V-670, JASCO, USA) over a wavelength range of 300–1200 nm. The excitation and photoluminescence (PL) spectra were measured with a photoluminescence spectrometer (iHR320, HORIBA Ltd., France); the excitation wavelength was 350 nm. X-ray photoelectron spectroscopy (XPS) was performed with a K-alpha XPS system (Thermo Fisher Scientific Inc., UK) using a monochromated Al Kα X-ray source with an energy of 1486.6 eV. The spectra of the Yb 4d and O 1s energy levels were calibrated with respect to the C 1s peak at 285.0 eV of the adventitious carbon that had formed on the substrate's surface. The oxide nanodots used for the optical measurements and XPS analysis were prepared with an $YbCl_3{\cdot}6H_2O$/4VP molar ratio of 0.3 and annealed under the same conditions used for the photoanode fabrication.

2.3. DSSC fabrication and characterization

TiO_2 photoanodes were screen-printed on ytterbium oxide nanodot arrays, which were formed on FTO:glass substrates. TiO_2 photoanodes on bare FTO:glass substrates were also fabricated for a control experiment. The resulting layers were dried for 10 min at 300 °C on a preheated hot plate. The screen printing and drying processes were repeated until a thickness of approximately 20 μm was obtained. Subsequently, the thick TiO_2 films were placed in a muffle furnace and gradually heated to 300 °C over a 30 min period, heated at 300 °C for 1 h, heated to 575 °C over a 30 min period, sintered at 575 °C for 1 h, and then cooled to room temperature. The active area of the electrodes was 0.25 cm^2. The prepared photoanodes were immersed in a 0.04 M solution of $TiCl_4$ at 75 °C for 1 h, rinsed with deionized water, and then sintered at 500 °C for 30 min. They were exposed to O_2 plasma for 10 min and then immersed for 24 h in one of two photosensitizer-containing ethanol solutions (0.5 mM) (either (cis-diisothiocyanato-bis(2,2-bipyridyl-4,4′-dicarboxylato)ruthenium(II) bis-(tetrabutylammonium), N719, Solaronix, Switzerland, or 2-cyano-3-(5-((4-(dimethylamino)-phenyl)ethynyl)thiophen-2-yl)acrylic acid, CSD-01, Sooyang Chemtec, Korea) [21]. Fig. 1 shows the UV–vis spectra of the N719 and CSD-01 dyes recorded in *N*,*N*-dimethylformamide (DMF, 1×10^{-5} M). The Pt counter electrodes were prepared on the FTO-coated glass with magnetron sputtering after two holes were drilled in the glass. Both the dye-sensitized TiO_2 electrode and Pt counter electrode were sealed with a 60-μm-thick layer of Surlyn (Solarnoix, Switzerland). An ionic liquid electrolyte (0.60 M of butyl methyl imidazolium iodide, 0.03 M of I_2, 0.50 M of 4-tert-butylpyridine, and 0.1 M of guanidinium thiocyanate in an 85:15 (v/v) mixture of acetonitrile:valeronitrile) was injected into the rear side of the counter electrode. The photovoltaic characteristics of the devices under AM 1.5 illumination (equivalent to one sun, 1 kW/m^2) were investigated with a solar cell current–voltage (I–V) measurement system (K3000 LAB, McScience, Korea). The photocurrent density (J_{sc}), open-circuit voltage (V_{oc}), fill factor (FF), and power-conversion efficiency (η) were simultaneously measured.

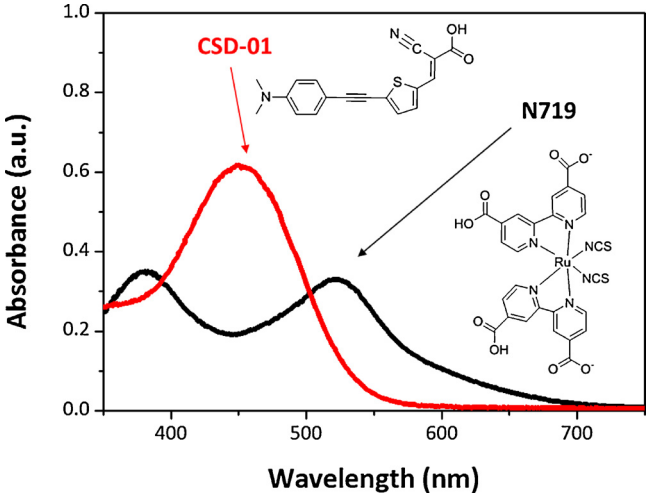

Fig. 1. Chemical structures and UV–vis absorbance spectra of the N719 (black spectrum) and CSD-01 (red spectrum) sensitizer molecules. (For interpretation of the references to color in this figure legend, the reader is referred to the web version of the article.)

3. Results and discussion

3.1. Self-ordered ytterbium oxide nanodots

Homogeneous spherical micelles were formed by using a 0.5 wt.% solution of the amphiphilic PS-*b*-P4VP copolymer in toluene. The Yb precursor was incorporated into the P4VP cores

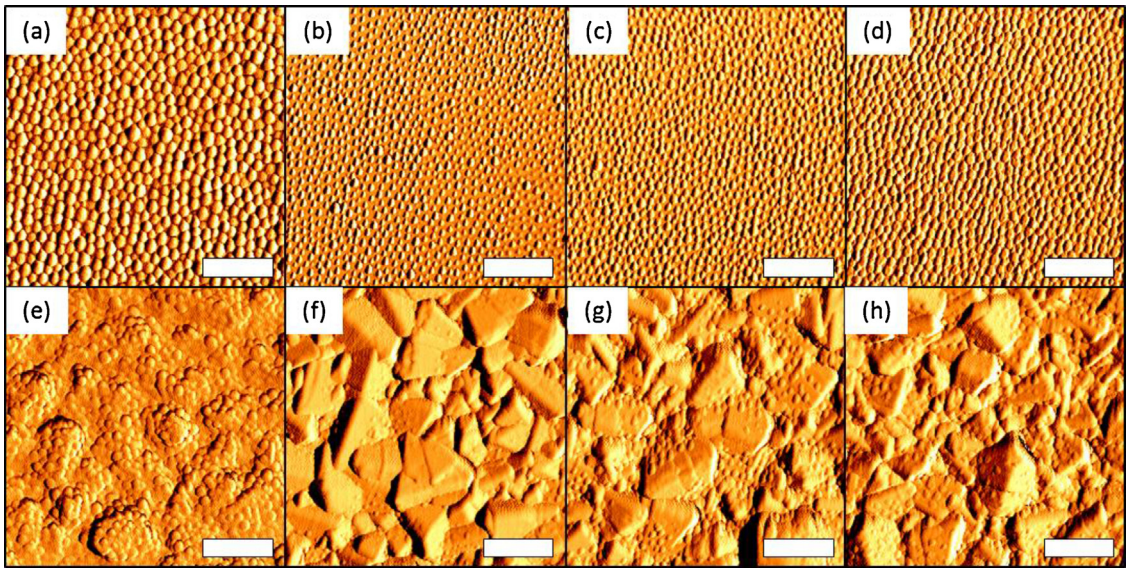

Fig. 2. Non-contact AFM phase images of the (a and e) as-prepared monolayers of the block copolymer thin films before the O_2 plasma treatment. The remaining non-contact AFM phase images show the (b and f) 0.1 mol, (c and g) 0.3 mol, and (d and h) 0.5 mol ytterbium oxide nanodot arrays after the O_2 plasma treatment. Si substrates were used for (a)–(d), and FTO-coated glass substrates were used for (e)–(h). The scale bars represent 500 nm.

Table 1
Average diameters and center-to-center distances of the 0.1, 0.3, and 0.5 mol layers of Yb_2O_3 nanodot arrays, which were measured from AFM images.

	0.1 mol	0.3 mol	0.5 mol
Diameter (nm)	35.27 ± 3.46	42.82 ± 6.88	50.08 ± 5.45
Center distance (nm)	64.62 ± 7.22	68.73 ± 8.52	68.39 ± 10.80

because of the favorable interactions between the Yb precursor and pyridine ring in the P4VP block. By controlling the concentration of PS-*b*-P4VP in the solution, a monolayer of the Yb-containing micelles were fabricated on either single-crystal Si or FTO-coated glass substrates with spin coating. Fig. 2 shows non-contact AFM phase images of the micellar films containing different concentrations of Yb before and after the O_2 plasma etching process. The non-contact AFM topographic images are provided in the Supplementary information (Fig. S1). Before the O_2 plasma treatment, quasi-hexagonal micellar arrays are present on the Si substrate. After the removal of the PS-*b*-P4VP templates, the trapped Yb precursor has been extricated and then oxidized to form the amorphous ytterbium oxide. The uniformity of the shape and size of the nanodots is slightly worse than that of the as-spun film because of the destructive nature of the O_2 plasma. Table 1 summarizes the average diameter of the nanodots and average center-to-center distance between the nanodots on the Si substrates. As the Yb concentration in the micelles increases, the size of the nanodots increases, but the center-to-center distance remains unchanged. This indicates that the size of the oxide nanodots can be controlled by loading the micelles with different concentrations of the Yb precursor and the distance between the nanodots can be altered by choosing a specific diblock copolymer. Unlike the Si substrate, the oxide nanodots have not formed a uniform layer on the FTO-coated glass substrates because the surface of the glass substrate is very rough ($R_{RMS} \approx 50.0$ nm). Even though fewer nanodots are present on the sharp edges of the underlying FTO crystals, the majority of the surface is covered, and thus, their photovoltaic functions should be unhindered.

3.2. XPS analysis

The chemical composition of the oxide nanodots that were thermally annealed under the same conditions as that of the photoanode fabrication process was confirmed with XPS measurements. According to the survey XPS spectrum (not shown), the nanodots contain Yb, O, and C. The presence of C may be caused by the diblock copolymer, the organic chemicals, or sample handling. The relative intensities of the XPS narrow scan spectra for the Yb 4d, O 1s, and C 1s states are shown in Fig. 3. The colored dash-dot lines in the XPS spectra denote the Lorentzian curves used to fit the spectra. The measured binding energies of the Yb 4d, O 1s, and C 1s states are summarized in Table 2. The Yb 4d spectrum in Fig. 3(a) has five main peaks between 180 and 210 eV, which are caused by the multiplet coupling in ytterbium sesquioxide (Yb_2O_3) [22]. The most intense peaks at 199.5 eV and 185.2 eV are due to emissions from the $4d_{3/2}$ and $4d_{5/2}$ levels of the Yb atoms, respectively. These results are in excellent agreement with the literature values for Yb_2O_3 [23]. The O 1s spectrum in Fig. 3(b) has two different oxygen bonding states. The main peak centered on 530.6 eV can be attributed to lattice oxygen in the Yb_2O_3, whilst the minor peak centered on 532 eV can be attributed to OH groups and/or oxygen atoms bound to carbon [24]. The C 1s spectrum in Fig. 3(c) consists of three peaks with binding energies of 285 eV (C—C), 286.5 eV (C—O), and 289.0 eV (C═O). This is evidence of the existence of carbon impurities in the Yb_2O_3 nanodots. Additional XPS spectra of the Sn 3d and F 1s levels from the underlying FTO-coated substrate are given in Figs. S2(a) and (b), respectively.

3.3. Optical transmittance and photoluminescence analysis

During DSSC operation, the light passes through glass, the FTO electrode, and Yb_2O_3 nanodots before reaching the photosensitizers, and therefore, the effect of the nanodots on the optical properties of the substrate is investigated. The optical transmittance spectra of the substrates coated with different concentrations of the nanodots are shown in Fig. 4(a). It is clear that the nanodots enhance the optical transparency in both the visible and NIR regions of the spectrum, and the level of coverage affects the transparency. It should be noted that zero-dimensional high-refractive-index (n) nanostructures can confine incident light in the propagation direction (e.g., $n_{FTO} = 1.74$ and $n_{Yb2O3} = 1.94$ at 632.8 nm), and can scatter light with wavelengths much longer than the size of the nanoparticles by diffracting the incident light at oblique angles. In addition, the light trapped in a spherical geometry can be circulated around

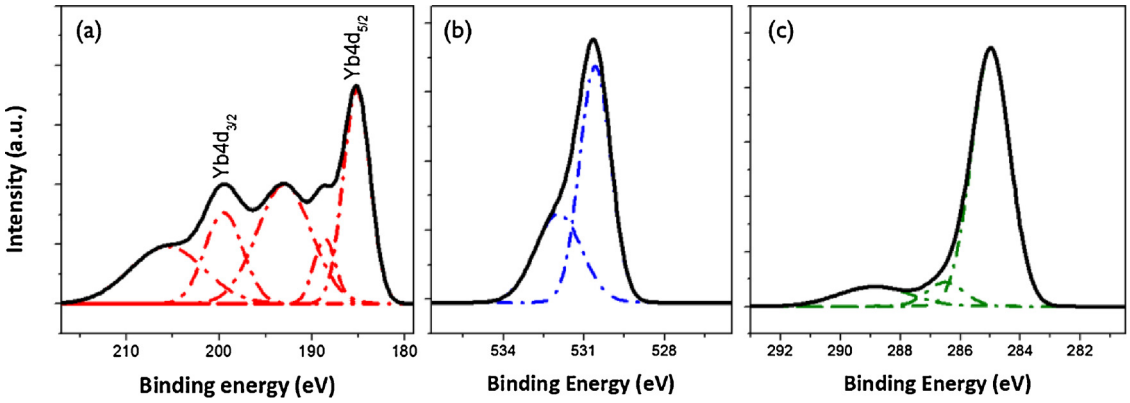

Fig. 3. Detailed XPS spectra of the (a) Yb 4d, (b) O 1s, and (c) C 1s levels. The colored dash-dot lines indicate the Lorentzian curves fitted to the experimental data. (For interpretation of the references to color in this figure legend, the reader is referred to the web version of the article.)

Table 2
The binding energies, and its sources, of the Yb 4d, O 1s, and C 1s levels present in the Yb_2O_3 nanodots, which were determined from the detailed XPS spectra in Fig. 3.

Yb 4d (eV)	205.6	199.5 $4d_{3/2}$	193.0	188.6	185.2 $4d_{5/2}$
O 1s (eV)	532.0 C—O	530.6 Yb—O			
C 1s (eV)	289.0 C=O	286.5 C—O	285.0 C—C		

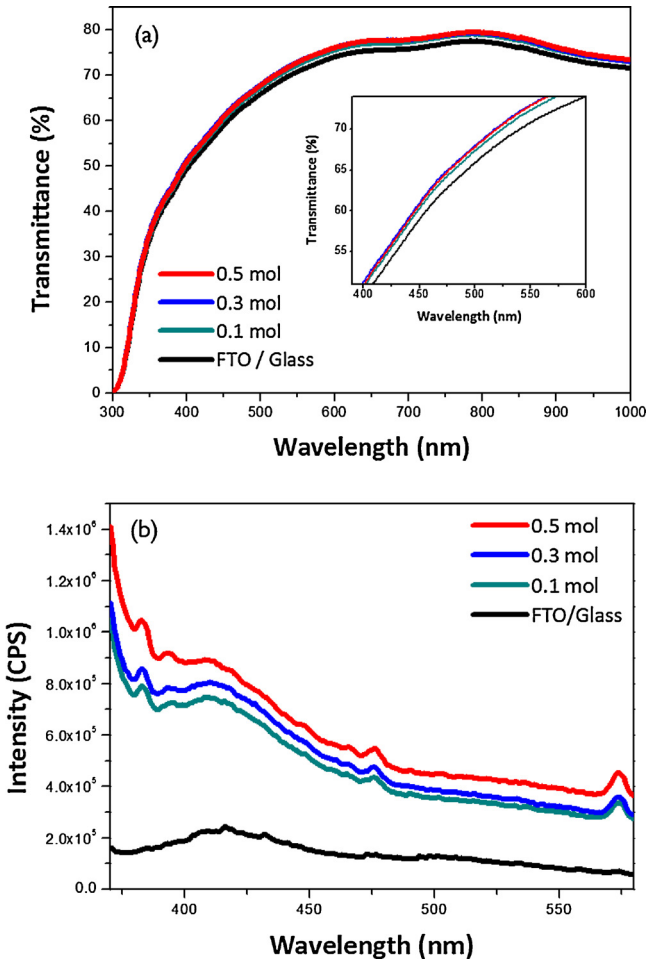

Fig. 4. (a) UV–vis and (b) PL spectra of the bare FTO-coated glass, and the FTO-coated glass samples with 0.1, 0.3, and 0.5 mol Yb_2O_3 nanodot coatings. The inset of (a) shows a magnified portion of transmittance spectrum.

the circumference of the system because of the multiple total internal reflections. Interestingly, when excited with UV light, the Yb_2O_3 nanodots on the substrate exhibit stronger emission intensities than that of the bare substrate (Fig. 4(b)). Recently, the Yb^{3+}-based cooperative up-conversion luminescence of Yb_2O_3 was reported, and white light was produced in a vacuum by the broad-band emission from Yb_2O_3 because of the four- and two-photon emission processes of Yb^{3+}–Yb^{3+} dimers and Yb^{2+}, respectively [25]. Although no down-conversion luminescence of Yb_2O_3 has been reported, some lanthanide sesquioxides (e.g., Y_2O_3, La_2O_3, and Gd_2O_3) have exhibited bluish-white emission when excited with UV light because of the defect centers associated with carbon impurities [26]. Therefore, it can be inferred from the results that the carbon from the diblock copolymers and organic chemicals affects the stoichiometry of the host lattice by forming carbon interstitial defects and/or oxygen vacancies. The resulting charge imbalances are rectified by the localization of electrons and holes, which creates photoluminescence through the strong electron-photon coupling [27,28].

3.4. Photovoltaic performance of the DSSCs

Fig. 5 shows the *J*–*V* characteristics of the DSSCs with and without the Yb_2O_3 nanodots. The photovoltaic parameters are summarized in Table 3. As the surface coverage of the Yb_2O_3 nanodots on the FTO electrode increases, the V_{oc} gradually increases; the V_{oc} increases from 0.723 V (N719, TiO_2 only) and 0.576 V (CSD-01, TiO_2 only) to 0.758 V (N719, 0.5 mol Yb_2O_3) and 0.619 V (CSD-01, 0.5 mol Yb_2O_3), respectively. These improvements in V_{oc} might originate from the nanodots preventing the loss of photoinjected electrons, which usually occurs through the back reaction with I_3^- via the FTO substrate, and suppressing the electron leakage between the FTO and nanocrystalline TiO_2 layers. This suggests that Yb_2O_3 can also act as a blocking material. However, both J_{sc} and η reach their maximum values when the molar ratio of $YbCl_3{\cdot}6H_2O$ to 4VP is 0.3; J_{sc} increases from 15.88 mA/cm^2 (N719, TiO_2 only) and 8.13 mA/cm^2 (CSD-01, TiO_2 only) to 16.11 mA/cm^2 (N719, 0.3 mol Yb_2O_3) and 9.54 mA/cm^2 (CSD-01, 0.3 mol Yb_2O_3), respectively. η increases from 6.07% (N719, TiO_2 only) and 3.02% (CSD-01, TiO_2 only) to 6.71% (N719, 0.3 mol Yb_2O_3) and 3.64% (CSD-01, 0.3 mol Yb_2O_3), respectively. The efficiencies are 10.5% (N719) and 20.5% (CSD-01) higher than that of the reference cells. This indicates the higher efficacy of Yb_2O_3 to CSD-01 than N719 because of strong luminescence of Yb_2O_3 in the lower wavelength region comparable with their absorption spectra (Fig. 1). However, even if the efficient capture of incident light (higher transmission, more internal reflections, and more photoluminescence) by the nanodots allows more electrons

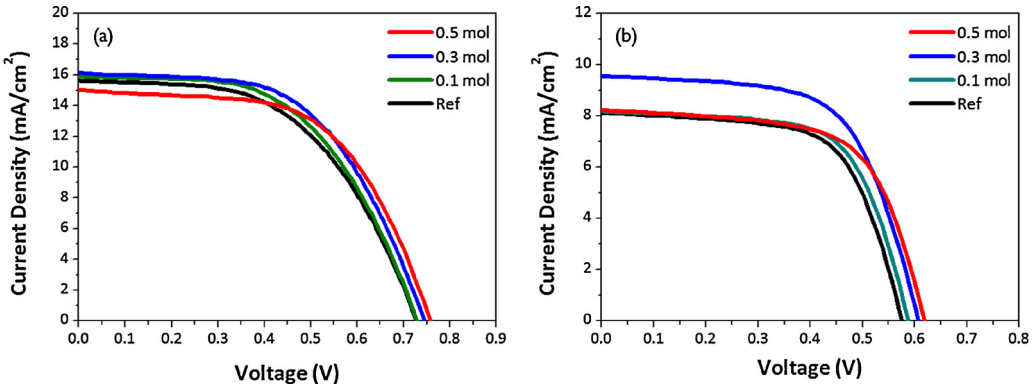

Fig. 5. *J–V* curves of the DSSCs with different concentrations of the Yb_2O_3 nanodot arrays for the two dyes tested: (a) N719 and (b) CSD-01.

Table 3
Photovoltaic parameters of the DSSCs with different concentrations of Yb_2O_3 nanodot arrays for both N719 and CSD-01 dyes.

	N719				CSD-01			
	J_{sc} (mA/cm^2)	V_{oc} (V)	FF (%)	η (%)	J_{sc} (mA/cm^2)	V_{oc} (V)	FF (%)	η (%)
Ref	15.88	0.723	52.7	6.07	8.13	0.576	64.4	3.02
0.10 mol	15.88	0.730	54.3	6.36	8.18	0.588	65.2	3.14
0.30 mol	16.11	0.745	56.0	6.71	9.54	0.607	62.8	3.64
0.50 mol	15.02	0.758	58.1	6.62	8.23	0.619	63.7	3.24

to be generated, an excessive coating of nanodots will negatively affect the photoelectron conversion process.

4. Conclusions

In this study, we have developed the novel phosphor, Yb_2O_3, and tested its applicability as a UV-absorbing spectral converter in DSSCs. We have also demonstrated the multifunctionality of the Yb_2O_3 nanodots, i.e., they can trap more light and prevent charge recombination at the interfaces in the DSSCs. Compared to DSSCs without the Yb_2O_3 nanodots, we found the power-conversion efficiencies for both Ru-based and organic dyes were improved by the presence of the nanodots. Currently, we are exploring the efficacy of other lanthanide sesquioxides for improving DSSC performance and we hope this paper will encourage such nanomaterials to be used to increase the light harvesting efficiency of DSSCs.

Acknowledgements

This work was supported by a Small and Medium Business Administration (SMBA) grant (no. S2129333) and National Research Foundation of Korea (NRF) grants funded by the Ministry of Science, ICT, and Future Planning of Korea (nos. 2013-026989 and 2014M3A9B8023478).

Appendix A. Supplementary data

Supplementary data associated with this article can be found, in the online version, at http://dx.doi.org/10.1016/j.apsusc.2015.12.077.

References

[1] A. Hagfeldt, G. Boschloo, L. Sun, L. Kloo, H. Petterson, Dye-sensitized solar cells, Chem. Rev. 110 (2010) 6595–6663.
[2] S. Zhang, X. Yang, Y. Numata, L. Han, High efficient dye-sensitized solar cells: progress and future challenges, Energy Environ. Sci. 6 (2013) 1443–1464.
[3] A. Fakharuddin, R. Jose, T.M. Brown, F. Fabregat-Santiago, J. Bisquert, A perspective on the production of dye-sensitized solar modules, Energy Environ. Sci. 7 (2014) 3952–3981.
[4] Md.K. Nazeeruddin, S.M. Zakeerudin, J.-J. Lagref, P. Liska, P. Comte, C. Barolo, G. Viscardi, K. Schenk, M. Grätzel, Stepwide assembly of amphiphilic ruthenium sensitizers and their applications in dye-sensitized solar cell, Coord. Chem. Rev. 248 (2004) 1317–1328.
[5] A. Mishra, M.K.R. Fischer, P. Bäuerle, Metal-free organic dyes for dye-sensitized solar cells: from structure: property relationships to design rules, Angew. Chem. Int. Ed. 48 (2009) 2474–2499.
[6] L.-L. Li, E.W.-G. Diau, Porphyrin-sensitized solar cells, Chem. Soc. Rev. 42 (2013) 291–304.
[7] H.A. Atwater, A. Polman, Plasmonics for improved photovoltaic devices, Nat Mater. 9 (2010) 205–213.
[8] N. Tétreault, M. Grätzel, Novel nanostructures for next generation dye-sensitized solar cells, Energy Environ. Sci. 5 (2012) 8506–8516.
[9] Q. Zhang, D. Myers, J. Lan, S.A. Jenekhe, G. Cao, Application of light scattering in dye-sensitized solar cells, Phys. Chem. Chem. Phys. 14 (2012) 14982–14998.
[10] J. Maçaira, L. Andrade, A. Mendas, Review on nanostructured photoelectrodes for next generation dye-sensitized solar cells, Renew. Sust. Energ. Rev. 27 (2013) 334–349.
[11] X. Huang, S. Han, W. Huang, X. Liu, Enhancing solar cell efficiency the search for luminescent materials as spectral converters, Chem. Soc. Rev. 42 (2013) 173–201.
[12] J. Wu, J. Wang, J. Lin, Y. Xiao, G. Yue, M. Huang, Z. Lan, Y. Huang, L. Fan, S. Yin, T. Sato, Dual functions of YF_3:Eu^{3+} for improving photovoltaic performance of dye-sensitized solar cells, Sci. Rep. 3 (2013) 2058 (1–5).
[13] J. Zhang, H. Shen, W. Guo, S. Wang, C. Zhu, F. Xue, J. Hou, H. Su, Z. Yuan, An upconversion $NaYF_4$:Yb^{3+},Er^{3+}/TiO_2 core–shell nanoparticle photoelectrode for improved efficiencies of dye-sensitized solar cells, J. Power Sources 226 (2013) 47–53.
[14] M.L. Brongersma, Y. Cui, S. Fan, Light management for photovoltaics using high-index nanostructures, Nat. Mater. 13 (2014) 451–460.
[15] I.W. Hamley, Nanostructure fabrication using block copolymers, Nanotechnology 14 (2003) R39–R54.
[16] C. Park, J. Yoon, E.L. Thomas, Enabling nanotechnology with self assembled block copolymer patterns, Polymer 44 (2003) 6725–6760.
[17] M. Lazzari, M.A. López-Quintela, Block copolymers as a tool for nanomaterial fabrication, Adv. Mater. 15 (2003) 1583–1594.
[18] T. Lohmueller, E. Bock, J.P. Spatz, Synthesis of quasi-hexagonal ordered arrays of metallic nanoparticles with tunable particle size, Adv. Mater. 20 (2008) 2297–2302.
[19] S.P. Anthony, W.J. Cho, J.I. Lee, J.K. Kim, Synthesis of lead chalcogenide nanoparticles in block copolymer micelles: investigation of optical properties and fabrication of 2-D arrays of nanoparticles, J. Mater. Chem. 19 (2009) 280–285.
[20] J. Kim, J. Hong, M. Park, W. Zhe, D. Kim, Y.J. Jang, D.H. Kim, K. No, Facile preparation of PbTiO3 nanodot arrays: combining nanohybridization with vapor phase reaction sputtering, Adv. Funct. Mater. 21 (2011) 4277–4284.
[21] M. Al-Eid, S.H. Lim, K.-W. Park, B. Fitzpatrick, C.-H. Han, K. Kwak, J. Hong, G. Cooke, Facile synthesis of metal-free organic dyes featuring a thienylethynyl spacer for dye sensitized solar cells, Dyes Pigm. 104 (2014) 197–203.
[22] A. Kotani, H. Ogasawara, Theory of core-level spectroscopy of rare-earth oxides, J. Electron Spectrosc. Relat. Phenom. 60 (1992) 257–299.

[23] S.B.M. Hagström, P.O. Hedén, H. Löfgren, Electron density of states in Yb metal as observed by X-ray photoemission, Solid State Commun. 8 (1970) 1245–1248.
[24] D.H. Kim, Z. Sun, T.P. Russell, W. Knoll, J.S. Gutmann, Organic–inorganic nanohybridization by block copolymer thin films, Adv. Funct. Mater. 15 (2005) 1160–1164.
[25] J. Wang, P.A. Tanner, Upconversion for white light generation by a single compound, J. Am. Chem. Soc. 132 (2010) 947–949.
[26] C. Lin, C. Zhang, J. Lin, Sol–gel derived Y_2O_3 as an efficient bluish-white phosphor without metal activator ions, J. Lumin. 129 (2009) 1469–1474.
[27] T. Hayakawa, A. Hiramitsu, M. Nogami, White light emission from radical carbonyl-terminations in Al_2O_3–SiO_2 porous glasses with high luminescence quantum efficiencies, Appl. Phys. Lett. 82 (2003) 2975–2977.
[28] Y.C. Lee, Y.L. Liu, J.L. Shen, I.J. Hsu, P.W. Cheng, C.F. Cheng, C.H. Ko, Blue-green luminescence from mesoporous MCM-48 molecular sieves, J. Non-Cryst. Solids 341 (2004) 16–20.